

Mantle dynamics of the North China Craton: new insights from mantle transition zone imaging constrained by *P*-to-*S* receiver functions

Lin Liu^{1b},^{1,2,3,4} Stephen S. Gao^{1b},² Kelly H. Liu,² William L. Griffin,⁵ Sanzhong Li,^{1,4} Siyou Tong^{1,4} and Jieyuan Ning⁶

¹Frontiers Science Center for Deep Ocean Multispheres and Earth System, Key Lab of Submarine Geosciences and Prospecting Techniques, MOE, and College of Marine Geosciences, Ocean University of China, Qingdao 266100, China. Email: lltc@mst.edu

²Geology and Geophysics Program, Missouri University of Science and Technology, Rolla, MO 65409, USA

³Department of Geophysics, Stanford University, Stanford, CA 94305, USA

⁴Laboratory for Marine Mineral Resources, Qingdao National Laboratory for Marine Science and Technology, Qingdao 266237, China

⁵Australian Research Council Centre of Excellence for Core to Crust Fluid Systems (CCFS)/GEMOC, Earth and Planetary Sciences, Macquarie University, Sydney, NSW 2109, Australia

⁶Institute of Theoretical and Applied Geophysics, School of Earth and Space Science, Peking University, Beijing 100871, China

Accepted 2022 June 6. Received 2022 April 25; in original form 2021 September 28

SUMMARY

Cratons are generally defined as stable continental blocks with a strong cratonic root that typically is at least ~200 km thick. Many cratons have undergone little internal tectonism and destruction since their formation, but some of them, such as the eastern part of the North China Craton (NCC), the Dharwar Craton and the Wyoming Craton, have lost their thick cratonic root and become reactivated in recent geological history, leading to widespread Meso-Cenozoic volcanisms. The mechanisms responsible for such decratonization remain debated. To provide new constraints on models leading to decratonization, in this study we stack 612 854 source-normalized *P*-to-*S* conversions (receiver functions or RFs) from the 410 and 660 km discontinuities (d410 and d660, respectively) bordering the mantle transition zone (MTZ) recorded at 1986 stations in the NCC. Both the number of RFs and the number of stations are unprecedented in the study area. The average apparent depths of the d410 and d660 and the thickness of the MTZ are 413 ± 6 , 669 ± 8 and 255 ± 6 km, respectively. A depression of up to 37 km and mean 11 km of the d660 are clearly observed beneath the eastern NCC, mainly caused by the possible existence of a relatively large amount of water in the MTZ. Our study provides strong observational evidence for geodynamic modelling that suggests water in the MTZ can be driven out into the upper mantle by poloidal mantle flow induced by the subduction and retreat of subducted oceanic slabs. The results are consistent with the weakening of the lithosphere beneath the eastern NCC by the release of water (in the form of structurally bound H/OH) brought down to the MTZ by subduction of the Pacific slab. Continuous slab dehydration and the ascent of fluids would have triggered intraplate volcanism and mantle upwelling in the eastern NCC, as evidenced by the spatial correspondence among the lower-than-normal upper-mantle seismic velocities, unusually large depressions of the d660, Cenozoic basaltic volcanism and thinning of the cratonic lithosphere.

Key words: Asia; Body waves; Cratons; Dynamics: seismotectonics; Subduction zone processes.

1 INTRODUCTION

Mineral physics experiments predict that cold and mature (≥ 50 Myr) slabs can carry water into the mantle transition zone (MTZ) in hydrous minerals and dense hydrous magnesium silicates

(Thompson 1992; Pearson *et al.* 2014). It is generally hypothesized that the subducted water stays in the MTZ and in a 1–10 km thick layer of super-saturation that contains about 10 wt percent of water in the melt immediately above the 410-km discontinuity (d410, Bercovici & Karato 2003). A recent modelling study (Yang

& Faccenda 2020), however, suggests that poloidal flow induced by slab subduction and retreat can induce water in the MTZ being released into the upper mantle, leading to upper-mantle hydration and intraplate volcanism in NE China. Some previous seismic tomography studies have revealed the existence of high-velocity anomalies in the MTZ that are interpreted as the stagnant Pacific slab beneath portions of the North China Craton (NCC, Li *et al.* 2008; Liu *et al.* 2017). However, the spatial distribution of the low-velocity anomalies and the Cenozoic magmatism are not well correlated, probably due to the limited resolution of the tomographic images in the MTZ, as suggested by the large discrepancies among different tomography studies (Li *et al.* 2008; Lei 2012; Obayashi *et al.* 2013; Lei & Zhao 2016; Lu *et al.* 2019). Although the cold subducted slab possesses higher velocity than surrounding mantle materials, progressive heating of the subducted slab gradually reduces the velocity contrast between the slab and the ambient mantle (Foulger *et al.* 2013). Besides, it is generally accepted that hydration results in low seismic velocity at ambient pressure (Mao *et al.* 2012). Thus, the presence of subduction and abundance water might lead to normal or even subnormal velocities in the slabs and surrounding regions of the mantle if the effects of hydration and heating of the subducted slab exceed that of the low temperature of the slab (Foulger *et al.* 2013).

The topography of the d410 and d660 seismic discontinuities can reveal the presence of fluid in the MTZ and the effects of *in situ* temperature (Ringwood 1975; Thio *et al.* 2016). The d410 represents the phase transition from olivine to wadsleyite, which has a positive Clapeyron slope, such that a low-temperature zone corresponds to an uplift of the d410 and vice versa. On the contrary, the d660 represents the phase change from ringwoodite to bridgmanite and ferropericlase, which has a negative Clapeyron slope (Ringwood 1975). Under abnormally high-temperature conditions (above 1800 K), the minerals at the d660 are dominated by the phase transition from majorite garnet to perovskite (Hirose 2002), leading to a positive Clapeyron slope. Recent experimental results (Ghosh *et al.* 2013) propose that water plays a role similar to low temperature in the topography of the MTZ discontinuities (Litasov *et al.* 2005). For instance, under wet conditions at 1473 K, the phase transformation of the d410 shifts to lower pressures, while that of the d660 shifts to higher pressures, uplifting the d410 and depressing the d660, respectively (Litasov *et al.* 2005). However, it is difficult to distinguish thermal and water effects due to the average velocities and densities variation with water content and temperature in the MTZ, thus the conventional observation of low-wave speed and thicker MTZ for water and low-wave speed and thin MTZ for high temperature should be treated with caution (Thio *et al.* 2016). Controversy exists regarding the actual magnitude of the Clapeyron slopes, especially for the d660 (Ghosh *et al.* 2013). The Clapeyron slope for transition of hydrous Mg_2SiO_4 is between -3.2 and -3.1 $MPa K^{-1}$ (Ghosh *et al.* 2013), much steeper than that of anhydrous Mg_2SiO_4 (-0.7 to -0.4 $MPa K^{-1}$; Tsuchiya 2003) and hydrous pyrolyte (-2.2 $MPa K^{-1}$; Litasov *et al.* 2005). Consequently, significant depression of the d660 is indicative of the presence of a fluid-rich MTZ due to the gentle Clapeyron slope in the anhydrous phase transition mentioned above (Ghosh *et al.* 2013). It has been proposed that under normal conditions, a dense low-velocity layer (LVL) rich in water or partial melts that were vertically transported from the hydrous MTZ is trapped above the d410 globally (usually between 350 and 410 km; Bercovici & Karato 2003), because of the greatly reduced water storage capacity of the lowermost upper mantle relative to the MTZ.

A number of MTZ studies using *P*-to-*S* receiver functions (RFs) have been carried out in the NCC to investigate the thermal and water

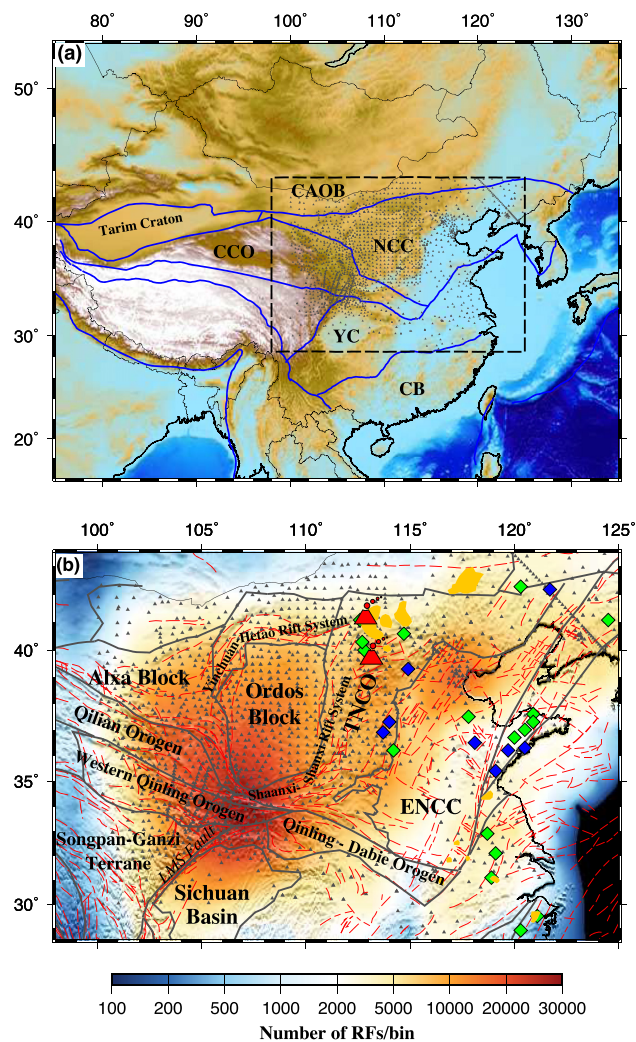


Figure 1. (a) Topographic map depicting the distribution of seismic stations (grey triangles) and major tectonic features within and around the study region. The black dash line outlines our study area in (b). NCC: North China Craton; YC: Yangtze Craton; CB: Cathaysia Block; CAOB: Central Asian Orogenic Belt; CCO: Central China Orogen. (b) Spatial distribution of the number of well-defined RFs per circular bin with a radius of 1° . The localities of Mesozoic xenoliths, Cenozoic xenoliths, basalts and volcanoes are marked by blue diamonds, green diamonds, small yellow symbols and red triangles, respectively (Wu *et al.* 2019). The thin red dashed lines represent faults. LMS Fault: Longmenshan Fault. TNCO: Trans-North China Orogen; ENCC: Eastern North China Craton.

content anomalies in the vicinity of the MTZ and their relationships with crustal and mantle structure (Shen *et al.* 2008; Chen & Ai 2009; Wang & Niu 2011; Xu *et al.* 2011; Si *et al.* 2016; Sun *et al.* 2020). A significant depression (> 25 km) of the d660 beneath most of the eastern NCC and a double d660 beneath the southeastern NCC have been observed (Chen & Ai 2009; Wang & Niu 2011; Si *et al.* 2016). These complicated structures have been attributed to the subduction and stagnancy of the Pacific slab in the MTZ beneath the eastern part of the NCC. The slightly depressed d410 observed adjacent to the Datong volcano is proposed to be caused by localized low velocities above the d410 (Wang & Niu 2011; Xu *et al.* 2011).

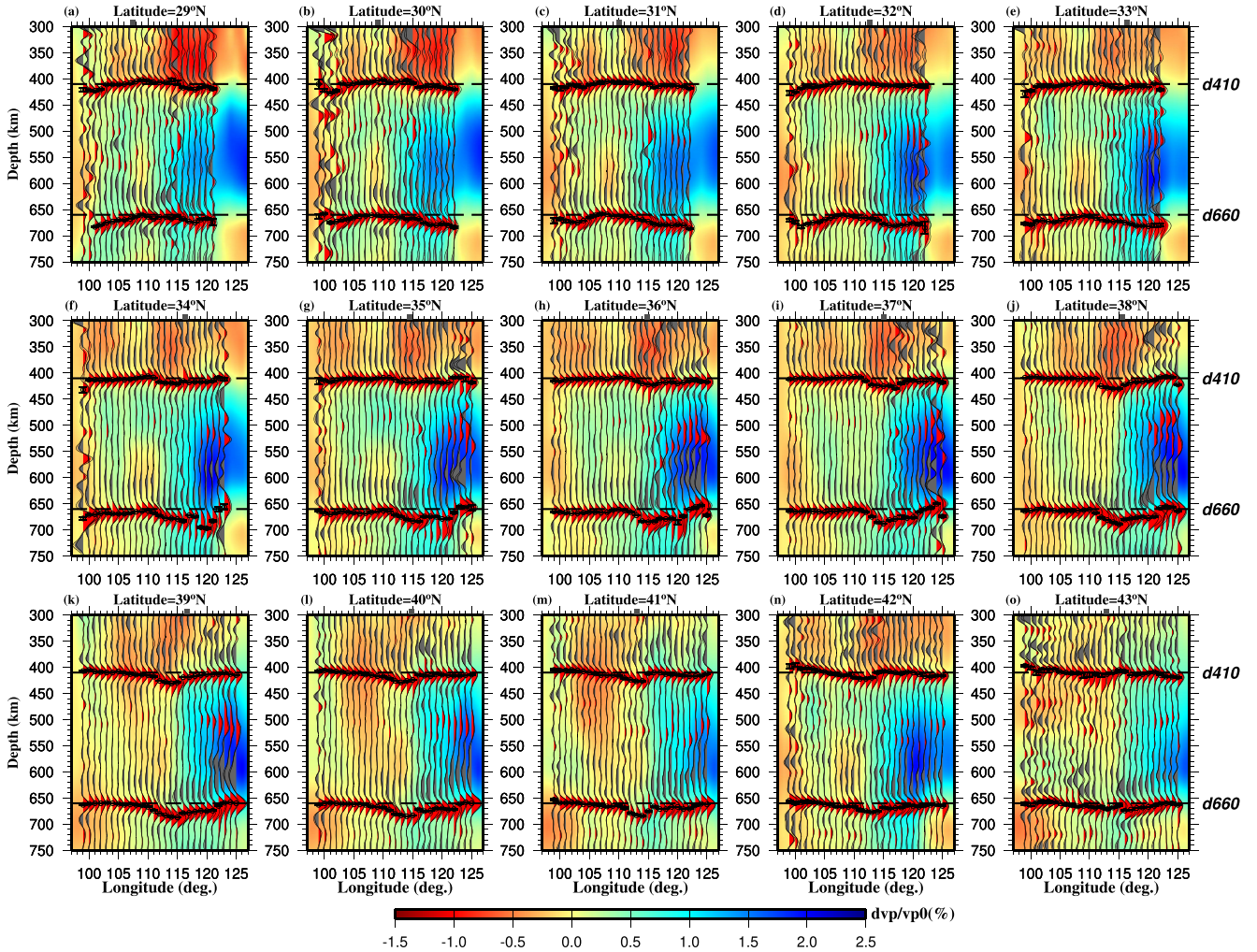


Figure 2. Results of stacked RFs in 1° circular bins along 15 latitudinal profiles, with P -wave anomalies as the background (Lu *et al.* 2019). For each bin, the bordering thin black lines indicate the depth series \pm standard deviations. The circles and bars show the resulting apparent depths of the MTZ discontinuities and standard deviations. The grey square at the top of each profile marks the boundary between regions A and B along that latitude.

The current investigation was motivated by the following factors. First, the recent availability of data from more than 1000 ChinArray broadband seismic stations provides greatly increased coverage and resolution for MTZ imaging in the NCC. Second, there is considerable controversy surrounding the spatial correlation between the stagnant Pacific slab in the MTZ and the low-velocity anomalies in the upper mantle and magmatism on the surface (Li *et al.* 2008; Lei 2012; Obayashi *et al.* 2013; Lei & Zhao 2016; Lu *et al.* 2019), due to the limited vertical resolution of tomographic techniques below 200 km. Third, although the hypothesis of subduction-induced delamination and accompanied volcanism has been proposed previously (Niu 2005; Chen & Ai 2009; Wang & Niu 2011; Xu *et al.* 2011; Si *et al.* 2016; Sun *et al.* 2020), specific processes leading to such delamination remain debated as mantle plume, rifting and slab dehydration could all result in lithospheric delamination and volcanism. Here, we use an unprecedentedly large number (612 854) of RFs and a non-plane-wave, nonlinear stacking procedure (Gao & Liu 2014b) to produce robust images of the MTZ discontinuities in circular bins of radius = 1° beneath the NCC and adjacent areas (Fig. 1), to provide additional constraints on the thermal properties and water-content distribution in the MTZ.

2 DATA AND METHOD

2.1 Data acquisition and selection

All the three-component broadband seismic waveform data for this study were recorded by 1986 densely spaced broadband seismic stations belonging to two station deployments (Fig. 1). Data recorded by 1162 stations are from the ChinArray program (ChinArray 2006) from the period between 2009 November and 2017 July. Another 824 stations, with data provided by the Data Management Center of China National Seismic Network at Institute of Geophysics of the China Earthquake Administration (Zheng *et al.* 2010), cover the period of 2007 July–2019 August. Teleseismic events with cut-off magnitudes greater than 5.5 and epicentral distance ranging from 30° to 100° are selected to calculate the RFs.

The seismograms are cut 20 s before and 260 s after the theoretical P -wave arrival and are filtered by a Bessel filter with a pass band of 0.02–0.2 Hz. The signal-to-noise ratio (S/N) is calculated through the function $S_1 = \max|A_s|/|\bar{A}_n|$, where $\max|A_s|$ is the maximum absolute value of the seismogram on the vertical component in the time window of 8 s before and 12 s after the predicted IASP91 (Kennett & Engdahl 1991) P -wave arrival time and $|\bar{A}_n|$ is the

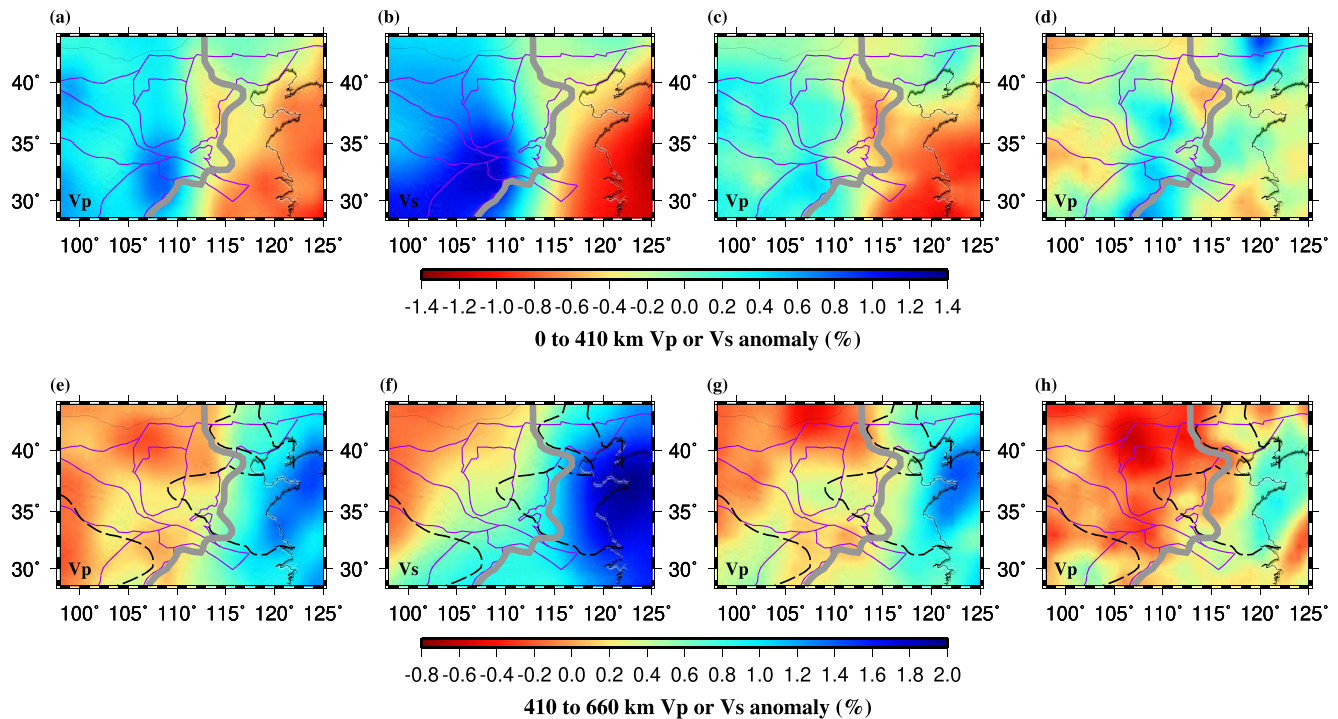


Figure 3. (a) Mean P -wave speed perturbations with respect to the AK135 model above the d410 (Lu *et al.* 2019). (b) Same as (a) but for S wave. (c) Same as (a), but from Obayashi *et al.* (2013). (d) Same as (a), but for Li *et al.* (2008). (e) Same as (a), but from the depth range between d410 and d660. (f) Same as (e), but for S wave. (g) Same as (e), but from Obayashi *et al.* (2013). (h) Same as (e), but from Li *et al.* (2008). Black dash lines outline the stagnant Pacific slab in the depth of 600 km detected by tomographic image of Lei (2012) and Lei & Zhao (2016).

average absolute value of the seismogram in the time window of 10–20 s before the predicted arrival time. Using the procedure of Ammon (1991), filtered seismograms with an S/N of 4.0 or greater on the vertical component are deconvoluted into radial RFs. To minimize the degenerating influence of the strong PP arrivals on the resulting RFs, the seismograms are pre-processed by an exponential weighting function with a half-width of 30 s centred on the PP theoretical arrival time (see Gao & Liu, 2014a for details). The functions are defined as

$$G(t) = \begin{cases} e^{-0.2(t-t_{pp}+30.0)} & \text{if } t_{pp} - 30.0 \text{ s} < t < t_{pp} - 5.0 \text{ s;} \\ 0 & \text{if } t_{pp} - 5.0 \text{ s} < t < t_{pp} + 5.0 \text{ s;} \\ e^{-0.2(-t+t_{pp}+30.0)} & \text{if } t_{pp} + 5.0 \text{ s} < t < t_{pp} + 30.0 \text{ s.} \end{cases}$$

Through the above function, the PP energy is reduced. Finally, a total of 612 854 well-defined RFs recorded by 1986 stations (Fig. 1) from 9319 events (Fig. S1, Supporting Information) are selected for our study.

2.2 Moveout correction, stacking and wave speed correction

Detailed descriptions of the procedure for data pre-processing, moveout correction, as well as stacking of P -to- S converted phase (Pds) arrivals under a non-plane-wave assumption can be found in the study of MTZ discontinuities for the contiguous United States (Gao & Liu 2014b), and are briefly described below. Rather than the common-conversion-point (CCP) approach (Dueker & Sheehan 1997), the assumption of a non-plane wave front is used for our study. The CCP approach assumes that the ray parameters of the direct P wave and the Pds phase generated from the MTZ discontinuities are the same, which introduces an error of a few kilometres

in the resulting depths and leads to less coherent stacking relative to the non-plane-wave approach (Lawrence & Shearer 2006; Gao & Liu 2014a).

The coordinates of the ray-piercing points at the depth of 535 km (which is approximately the centre of the MTZ globally) are first calculated. Then the RFs with piercing points in each of the radius = 1° circular bins are moveout-corrected using the IASP91 Earth model and stacked to form a depth series between 300 and 750 km with 1-km vertical resolution using $S(d) = \frac{1}{N} \sum_{i=1}^N S_i(t_i)$, where $S(d)$ is the stacking amplitude for a candidate discontinuity at the depth of d , N is the number of RFs in the circular bin, t_i is the non-plane wave moveout time of the i th RF at the depth of d calculated based on the IASP91 Earth model and $S_i(t_i)$ is the amplitude corresponding to the i th RF at time t_i . In the study area, the number of RFs per bin ranges from 16 to 29 934. The distance between neighbouring bins is 1° and therefore, there is an overlap among neighbouring bins.

Fig. 2 shows the resulting depth series along all the 15 latitudinal cross sections. The depths to the d410 and d660 are determined by picking the maximum value of stacking amplitude in the depth range of 380–440 and 630–690 km, respectively. The mean and standard deviation of the depths are obtained from 50 bootstrap resampling iterations using the procedure described by Liu *et al.* (2003). As a result of the high quality and quantity of the RFs, the d410 and d660 arrivals are unambiguously identified for virtually all the bins, including those on the edges of the study area (Fig. 2). Most bins exhibit an obvious negative arrival in the depth range from ~ 350 km to the positive arrivals corresponding to the d410. This LVL may represent the melting layer atop the d410 (Bercovici & Karato 2003; Tauzin *et al.* 2010; Wei & Shearer 2017), although

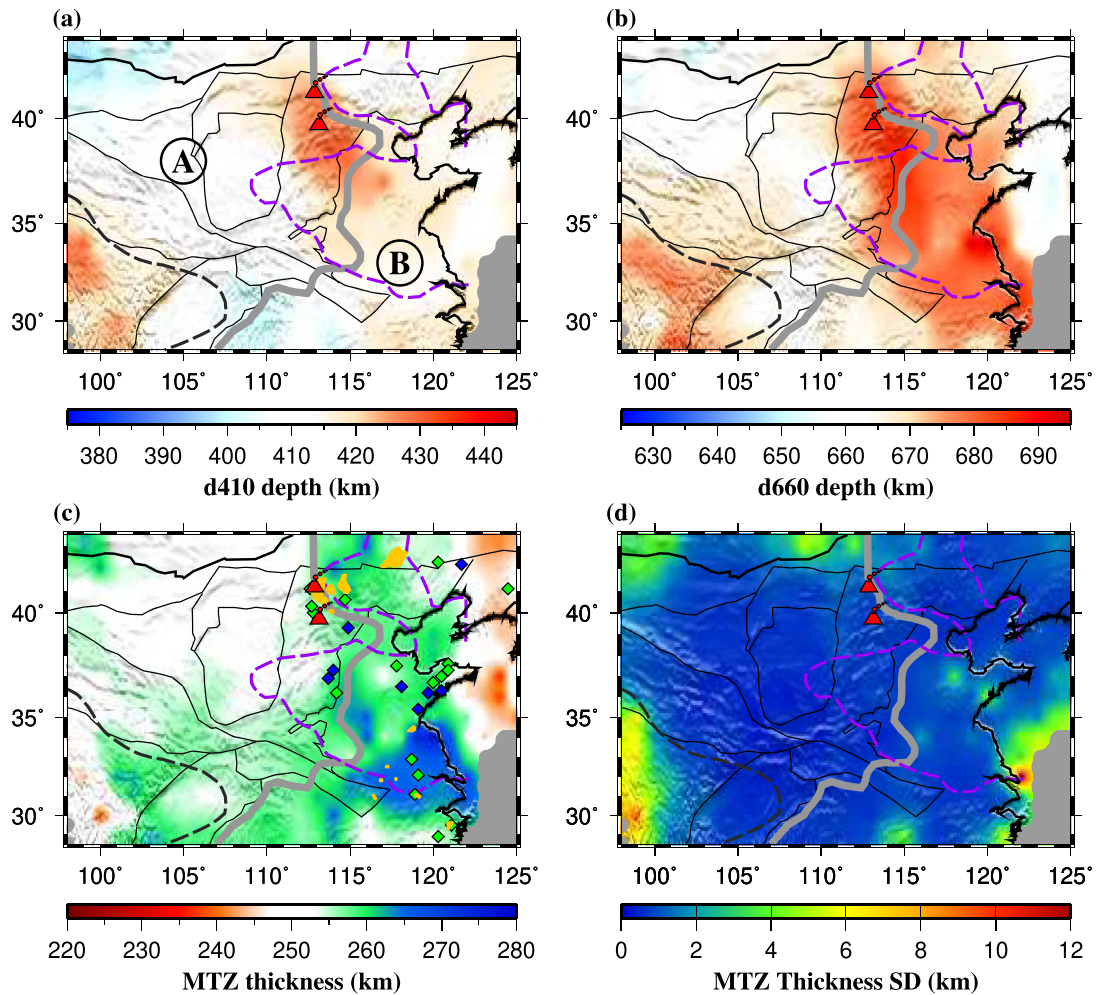


Figure 4. (a) Spatial distribution of resulting apparent d410 depths. (b) Same as (a), but for the d660. (c) MTZ apparent thickness measurements. (d) Standard deviation of the MTZ thickness measurements. Purple and black dash lines outline the stagnant Pacific slab and Burma slab in the depth of 600 km detected by tomographic images, respectively (Lei 2012; Lei & Zhao 2016). The grey thick line modified from Zhang *et al.* (2019) marks the western boundary of lithospheric thinning (~ 200 km to the west and < 110 km to the east) beneath the NCC (Fig. S2, Supporting Information). Results in 1° circular bins are resampled to 0.1° resolution.

Table 1. Mean apparent and corrected measurements for the entire study area and two subregions.

Area	d410 \pm σ_{d410} (km)	d660 \pm σ_{d660} (km)	MTZ \pm σ_{MTZ} (km)	Corrected d410 \pm σ_{d410} (km)	Corrected d660 \pm σ_{d660} (km)	Corrected MTZ $\pm \sigma_{MTZ}$ (km)
Entire area	413 \pm 6	669 \pm 8	255 \pm 6	415 \pm 6	674 \pm 8	259 \pm 7
A	413 \pm 7	667 \pm 7	254 \pm 4	417 \pm 6	673 \pm 8	256 \pm 5
B	414 \pm 5	671 \pm 9	257 \pm 7	412 \pm 4	674 \pm 8	262 \pm 8

the actual thickness of the layer cannot be determined convincingly due to the presence of multiple negative arrivals, weak amplitudes at many bins and possible interference with negative sidelobes of the positive d410 arrival.

The RFs, which are time series, are initially converted into depth series using the 1-D IASP91 standard Earth model, and thus the resulting discontinuity depths and MTZ thickness are apparent rather than true values. Velocity corrections are then performed to convert the apparent values into true values using TX2019slab, a global scale *P*- and *S*-wave velocity model (Lu *et al.* 2019) following the procedure in Gao & Liu (2014b). Relative to regional velocity models (Fig. 3), global models are more suitable for depth corrections

because regionally averaged background velocity anomalies are not removed.

3 RESULTS

In the study area of 98° – 125° E and 29° – 43° N, a total of 387 bins render robust determinations of d410 (387) and d660 (385). All the resulting stacked RFs in the 387 bins are plotted along 15 E-W profiles in Fig. 2. When the 1-D IASP91 Earth model is used for moveout correction and time–depth conversion, the resulting apparent depths of the MTZ discontinuities (Figs 4a and b; and Table 1) are positively correlated (0.67) for the study area (Fig. 5),

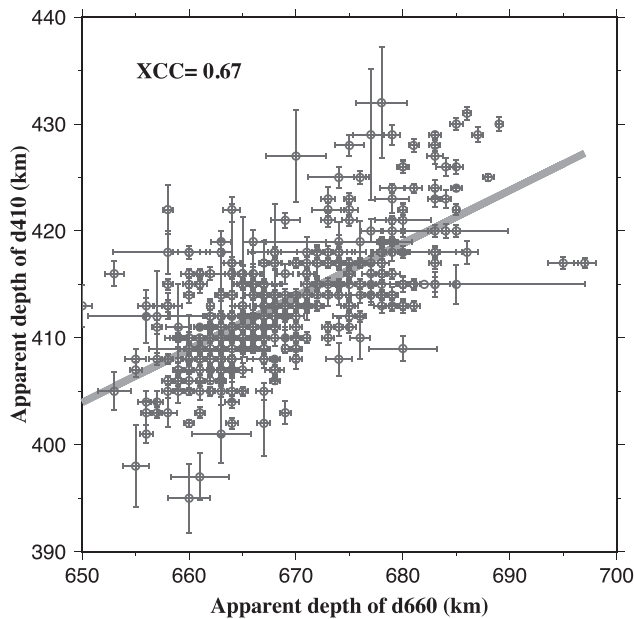


Figure 5. Correlation plot of apparent d410 versus d660 depths with standard deviation bars. The line indicates the optimal bivariate regression with a cross-correlation coefficient of 0.67.

suggesting that most of the observed undulations of the apparent depths reflect lateral variations of the average seismic velocity above the d410. Greater than normal apparent depths correspond to lower-than-normal upper mantle velocities, and vice versa. After a global velocity model (Figs 3a, b, e and 3f; Lu *et al.* 2019) being employed for velocity correction in the study area, the correlation coefficient between the corrected d410 and d660 depths is reduced to 0.59 from 0.67 (Fig. 5). The limited reduction reflects the low effectiveness of the velocity correction.

The apparent depths of the d410 range from 395 to 432 km with a mean of 413 ± 6 km, and the apparent depths of the d660 vary from 650 to 697 km with a mean of 669 ± 8 km, leading to a mean MTZ thickness of 255 ± 6 km (Fig. 4 and Table 1). The standard deviation of the MTZ thickness is less than 2 km for the majority of the study area (Fig. 4d), guaranteeing the reliability of main results. The mean amplitudes corresponding to the d410 and d660 (relative to that of the direct *P* wave, that is, $S(P410s)/S(P)$ and $S(P660s)/S(P)$) are 0.018 \pm 0.004 and 0.019 \pm 0.004, respectively (Table S1, Supporting Information). The corrected d410 depths (415 ± 6 km on average) are mostly within ± 5 km of the global values (Kennett & Engdahl 1991) and close to the apparent d410 depths, but the depression of the d660 remains significant or even more depressed (674 ± 8 km) and the corrected MTZ (259 ± 7 km) is thicker than the corresponding apparent values (Fig. 6 and Table 1).

Our study area is divided to Areas A and B (Fig. 4a) based on the 110 km depth contour of lithospheric thickness measured by Zhang *et al.* (2019) (Fig. S2, Supporting Information). Area A is located to the west of the boundary, where the lithospheric thickness is approximately 200 km. To the east of the boundary (Area B), where the lithospheric thickness is less than 110 km, both the d410 and d660 are apparently depressed (414 ± 5 and 671 ± 9 km), suggesting a lower-than-normal upper mantle velocity, which is consistent with the velocity anomalies obtained from seismic tomography studies (Figs 3a–c; and Fig. S3, Supporting Information). The apparent depression of the d660 (11 km on average) is greater than that of the

d410 (4 km on average), leading to an MTZ that is ~ 7 km thicker than normal (257 ± 7 km; Fig. 4 and Table 1). After velocity correction (Fig. 6 and Table 1, and Table S2, Supporting Information), the corrected d410 depth becomes close-to-normal (412 ± 4 km), while the corrected d660 is more depressed (674 ± 8 km).

4 DISCUSSIONS

4.1 Comparison with previous MTZ investigations

The differences in the MTZ between the western and eastern NCC are clearly illustrated by our RF results. The significantly depressed d660 (up to 37 km) and thickened MTZ (up to 30 km) beneath the eastern NCC are consistent with previous RF investigations that used fewer stations and thus had a lower spatial resolution (Shen *et al.* 2008; Chen & Ai 2009; Wang & Niu 2011; Xu *et al.* 2011; Si *et al.* 2016; Sun *et al.* 2020). Although these characteristics have been interpreted as related to the stagnation and sinking of the Pacific slab, details of their spatial distributions are controversial. For example, the thickened MTZ has been reported as distributed over the entire eastern NCC (Si *et al.* 2015; Wang & Niu 2011) or only over the southeastern part of the NCC (Chen & Ai 2009; Xu *et al.* 2011); the thickened MTZ is reported as either a continuous (Chen & Ai 2009; Xu *et al.* 2011) or localized feature (Si *et al.* 2015). Additionally, the double d660 beneath the southeastern NCC identified by some previous RF studies (Chen & Ai 2009; Wang & Niu 2011; Si *et al.* 2016) disappears when a greater number of RFs is used in our study (Fig. 2). Our increased number of RFs improves the S/N of resulting traces, excluding ‘fake’ discontinuities. This emphasizes the necessity of improvement of data coverage in determining reliable depths of the MTZ discontinuities and constraining their relationships to the subducted Pacific slab.

In the adjacent area of the NCC, such as NE China and SE China, numerous geophysical studies have been conducted to investigate the Pacific subduction slab. Sun *et al.* (2020), who mainly focused on MTZ imaging using RFs beneath NE Asia, presented a depression of the d660 in the northern part of the NCC. The depressed d660 to the east of the Datong volcanic field was explained by the dehydration of the stagnant Pacific slab in the MTZ. Wang *et al.* (2020) detected two internal discontinuities within the MTZ beneath NE China, interpreted as the Moho of the subducted oceanic slab and detached oceanic crust/partial melting of the slab, respectively. Comparing with our stacked RFs profiles in Fig. 2, analogous positive and negative phases can also be observed at depths between d410 and d660, especially from profiles of N36° to N41°. Taking profile N40° as example, the negative phase above the d660 is stronger and slightly dipping east of E117°, then it becomes weaker and flat west of E117°. These features are consistent with the spatial variations and the explanation for the origins of flattened (segregated oceanic crust) and dipping (partial melting of slab) sections beneath NE China in Wang *et al.* (2020). Feng *et al.* (2021) proposed that detached oceanic crust is trapped in the MTZ along profile N40°, based on joint analysis of reflected body waves retrieved from ambient noise interferometry and mineral physics modelling. The consistency of MTZ-related results between our work and other recent investigations in overlapping areas supports the reliability of our RF measurements. Our enhanced data coverage and larger study area provide high-resolution results and direct evidence for mantle dynamics induced by the subducted and stagnant Pacific slab.

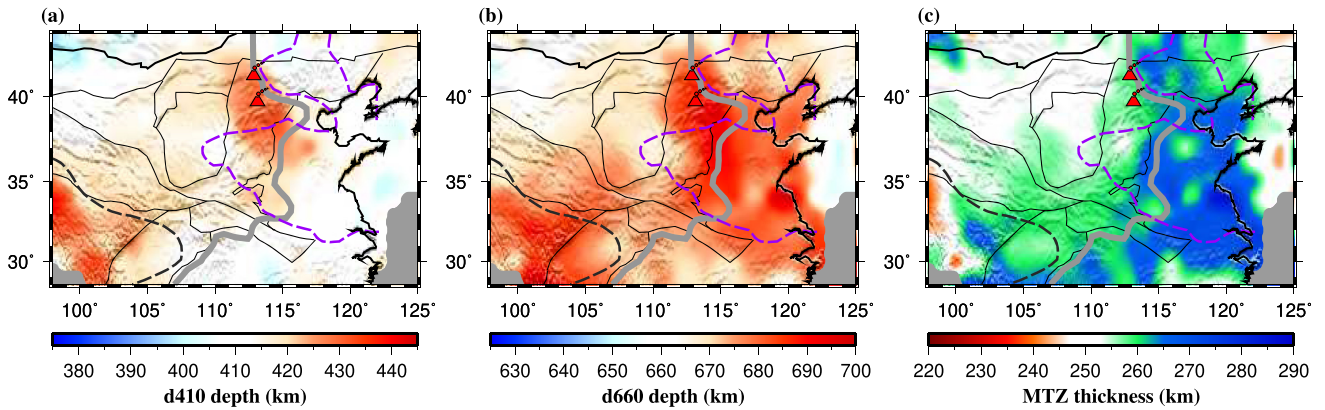


Figure 6. Same as Figs 4(a)–(c), but after corrections using the P - and S -wave speed models of Figs 3(a), (b), (e) and (f) (Lu *et al.* 2019).

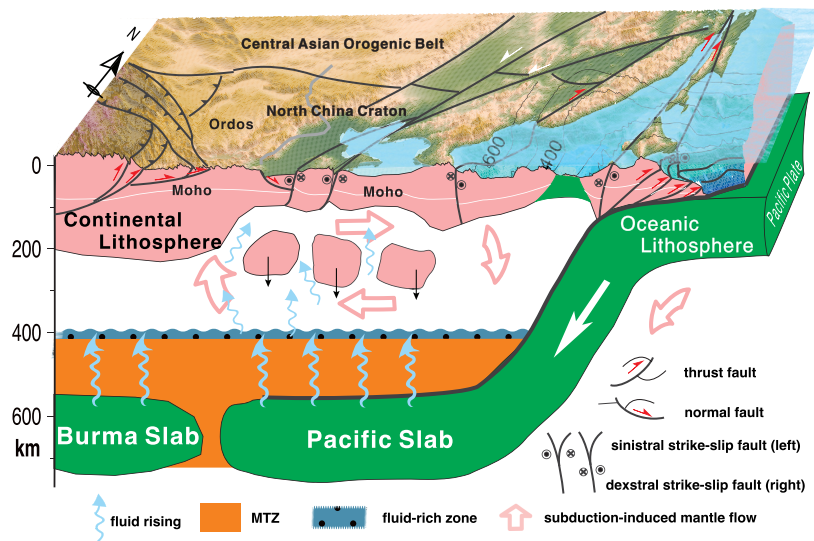


Figure 7. Schematic illustration showing the process of decratonization of the eastern NCC originating from MTZ dehydration in the Cenozoic.

4.2 Constraints on the mechanism of NCC reactivation

The lithosphere of the eastern NCC has experienced two phases of thinning/rifting in the Mesozoic and Cenozoic according to geothermal evidence (Qiu *et al.* 2014; Li *et al.* 2017). The spatial discrepancy of lithospheric thickness between Areas A and B has been constrained by S -to- P RfFs (Fig. S2, Supporting Information; Zhang *et al.* 2019). In addition, the stepwise thinning trend from the western to eastern NCC is confirmed in thermal and tomographic models (Liu *et al.* 2016; Yan *et al.* 2019), although various degrees of discrepancies in the resulting lithospheric thickness seems inevitable. Beneath Area B, most previous seismic tomography studies have revealed a high-velocity MTZ (Figs 3e–g; and Fig. S3, Supporting Information) and attributed it to the subducted Pacific slab (Li *et al.* 2008; Lei 2012; Obayashi *et al.* 2013; Lu *et al.* 2019). In contrast, the upper mantle above the d410 beneath Area B as seen in our study is characterized by low- rather than high-velocity anomalies (Figs 3a–c; and Fig. S3, Supporting Information). Our results reveal a remarkable coincidence of thickened MTZ and lower-than-normal velocities above the d410 beneath the eastern NCC. In addition, the area above the thickened MTZ is characterized by Meso-Cenozoic igneous activity (Fig. 1b) (Wu *et al.* 2019), considered to reflect asthenospheric upwelling accompanying the removal of lithospheric

mantle (Yang *et al.* 2008; Wu *et al.* 2019). The coexistence of a thickened MTZ, a thinned lithosphere, the recent intraplate volcanism, Cenozoic xenoliths/basalts and low upper-mantle velocities beneath the eastern NCC can be explained by the upwelling of fluids that originated from the dehydration of stagnant slabs (Fig. 7), as previously proposed to explain the Cenozoic volcanism and continental flood basalts across NE China (Yang & Faccenda 2020).

On the basis of plate reconstructions and subduction ages (Liu *et al.* 2017), the Mesozoic and Cenozoic episodes of lithosphere destruction are considered as being induced by the Palaeo-Pacific (Izanagi) and current Pacific plates, respectively. The mechanisms leading to the two phases of reactivation remain debated due to a lack of explicit evidence (Niu 2005). The current stagnant slab in the MTZ mostly belongs to the Pacific, rather than the Izanagi plate (Liu *et al.* 2017), thus our observations are mainly related to the second phase of lithospheric thinning event in the Cenozoic. The lithospheric age of the westward-subducting Pacific plate is 90–130 Ma (Liu *et al.* 2017), which is ancient enough to hydrate the MTZ (Thompson 1992; Pearson *et al.* 2014). The melting layer (LVL) atop the d410 (Bercovici & Karato 2003) would reflect the upwelling of water in the MTZ owing to the different H_2O storage capacities of the overlying mantle and the MTZ (Freitas *et al.* 2017).

Numerical simulations indicate that subduction and retreat of the Pacific slab would induce poloidal mantle flow, especially the vertical component of the flow system, and that this could carry at least 0.2–0.3 wt percent of water from the LVL and MTZ to the upper mantle (Yang & Faccenda 2020).

Water as H₂O does not exist in the deeper mantle, which is probably metal-saturated (Frost *et al.* 2004; Zhu *et al.* 2019). Instead, it is dissociated and stored as H in nominally anhydrous minerals (Wood *et al.* 1996). If these phases become saturated, the fluid phase promotes partial melting, and is dissolved in those melts (Revenaugh & Sipkin 1994; Freitas *et al.* 2017). The breakdown of hydrous phases in the MTZ also may release H directly, through dehydrogenation of subducted hydrous phases such as goethite (FeOOH, Hu *et al.* 2016). The mobility of hydrogen allows its rapid ascent through a metal-saturated mantle. On encountering the more oxidized lithospheric mantle, it will be re-oxidized to water, leading to metasomatism and partial melting, both of which will contribute to the destruction of the continental roots and intraplate volcanism (Wu *et al.* 2019). Our preferred model (Fig. 7) can account for the seismological and geochemical observations and geodynamical modelling results; it invokes the sinking of the refertilized, and thus densified, lithospheric root and the ascent of magma under the eastern NCC triggered by upwelling fluids that originated from the subducted Pacific slab. The Datong intraplate volcano above the western edge of the stagnant Pacific slab overlies the partially molten region in numerical experiments (Yang & Faccenda 2020), thus the volcanism could be initiated by the dehydration of the water-rich MTZ. The model agrees with the observation that the area with depressed d660 is spatially coincident with the area underlain by overall low-velocity upper mantle above the d410 (Figs 3a–d) and sporadic high-velocity bodies beneath the lithosphere, which might represent the detached lithospheric blocks (Lei 2012). This hypothesis of cratonic reactivation induced by dehydration of ancient oceanic plate provides a possible mechanism for the breakup of supercontinents, which is generally associated with mantle upwelling (Huang *et al.* 2019). Given the age consistency between the first phase of lithospheric weakening and the subducted Izanagi plate, it is possible that the first phase of reactivation in the Mesozoic was also related to slab dehydration.

5 CONCLUSIONS

The topography of the MTZ discontinuities beneath the NCC is imaged using an unprecedented amount of data from 1986 broadband seismic stations. Stacking of 612 854 individual RFs reveals a large-scale depression of the d660 by up to 37 km beneath the eastern NCC and close-to-normal MTZ thickness beneath the western NCC, indicating dehydration of stagnant Pacific slab in the MTZ of the eastern NCC. The mechanism and tectonic processes of reactivation of the NCC are revealed through integration of our RF results with previous geophysical and geodynamical analyses. The excellent spatial correspondence among the areas with inferred water in the MTZ, low-velocity upper mantle, basaltic volcanism, xenoliths and removal of the depleted cratonic lithosphere strongly implies that dehydration of the Pacific slab and upwelling of hydrous deep mantle from the MTZ is the ultimate cause of the decratonization of the eastern NCC.

ACKNOWLEDGMENTS

We thank Tianze Liu and Suzanne O'Reilly for valued suggestions. Constructive reviews from I. Bastow, S. Rost and an anonymous reviewer significantly improved the manuscript. This study is supported by the National Natural Science Foundation of China (91958214 and 42121005) and the Marine S&T Fund of Shandong Province for National Laboratory for Marine Science and Technology (Qingdao) (2022QNL050302) to SL, the National Natural Science Foundation of China (41874071) to JN and the U.S. National Science Foundation (1919789) to SG. This is contribution 1737 from the ARC Centre of Excellence for Core to Crust Fluid Systems (<http://www.ccfsmq.edu.au>) and 1506 in the GEMOC Key Centre (<http://www.gemocmq.edu.au>).

DATA AVAILABILITY

The data used in this study are available from Data Management Center of China Seismic Array and China National Seismic Network at Institute of Geophysics, China Earthquake Administration (last accessed in August 2019).

REFERENCES

- Ammon, C. J., 1991. The isolation of receiver effects from teleseismic P waveforms, *Bull. seism. Soc. Am.*, **81**(6), 2504–2510.
- Bercovici, D. & Karato, S. I., 2003. Whole-mantle convection and the transition-zone water filter, *Nature*, **425**, 39–44.
- Chen, L. & Ai, Y., 2009. Discontinuity structure of the mantle transition zone beneath the North China Craton from receiver function migration, *J. geophys. Res.—Solid Earth*, **114**(B6), doi:10.1029/2008JB006221.
- ChinArray, 2006. China Seismic Array waveform data: China Earthquake Administration, doi:10.12001/ChinArray.Data.
- Dueker, K. G. & Sheehan, A. F., 1997. Mantle discontinuity structure from midpoint stacks of converted P to S waves across the Yellowstone hotspot track, *J. geophys. Res.—Solid Earth*, **102**(B4), 8313–8327.
- Feng, J., Yao, H., Wang, Y., Poli, P. & Mao, Z., 2021. Segregated oceanic crust trapped at the bottom mantle transition zone revealed from ambient noise interferometry, *Nat. Commun.*, **12**(1), 1–8.
- Foulger, G. R., *et al.* 2013. Caveats on tomographic images, *Terra Nova*, **25**(4), 259–281.
- Freitas, D., Manthilake, G., Schiavi, F., Chantel, J., Bolfan-Casanova, N., Bouhifd, M. A. & Andraut, D., 2017. Experimental evidence supporting a global melt layer at the base of the Earth's upper mantle, *Nat. Commun.*, **8**, 2186, doi:10.1038/s41467-017-02275-9.
- Frost, D. J., Liebske, C., Langenhorst, F., McCammon, C. A., Trønnes, R. G. & Rubie, D. C., 2004. Experimental evidence for the existence of iron-rich metal in the Earth's lower mantle, *Nature*, **428**, 409–412.
- Gao, S. S. & Liu, K. H., 2014a. Imaging mantle discontinuities using multiply-reflected P-to-S conversions, *Earth planet. Sci. Lett.*, **402**, 99–106.
- Gao, S. S. & Liu, K. H., 2014b. Mantle transition zone discontinuities beneath the contiguous United States, *J. geophys. Res.—Solid Earth*, **119**(8), 6452–6468.
- Ghosh, S., Ohtani, E., Litasov, K. D., Suzuki, A., Dobson, D. & Funakoshi, K., 2013. Effect of water in depleted mantle on post-spinel transition and implication for 660 km seismic discontinuity, *Earth planet. Sci. Lett.*, **371–372**, 103–111.
- Hirose, K., 2002. Phase transitions in pyrolitic mantle around 670-km depth: implications for upwelling of plumes from the lower mantle, *J. geophys. Res.—Solid Earth*, **107**(B4), ECV 3–1–ECV 3–13.
- Hu, Q., Kim, D. Y., Yang, W., Yang, L., Meng, Y., Zhang, L. & Mao, H. K., 2016. FeO₂ and FeOOH under deep lower-mantle conditions and Earth's oxygen–hydrogen cycles, *Nature*, **534**, 241–244.
- Huang, C., Zhang, N., Li, Z.X., Ding, M., Dang, Z., Pourteau, A. & Zhong, S., 2019. Modeling the inception of supercontinent breakup: stress state

- and the importance of orogens, *Geochem. Geophys. Geosyst.*, **20**, 4830–4848.
- Kennett, B. L. N. & Engdahl, E. R., 1991. Traveltimes for global earthquake location and phase identification, *Geophys. J. Int.*, **105**(2), 429–465.
- Lawrence, J. & Shearer, P. M., 2006. A global study of transition zone thickness using receiver functions, *J. geophys. Res.*, **111**, n/a, doi:10.1029/2005JB003973.
- Lei, J., 2012. Upper-mantle tomography and dynamics beneath the North China Craton, *J. geophys. Res.—Solid Earth*, **117**(B6), n/a, doi:10.1029/2012JB009212.
- Lei, J. & Zhao, D., 2016. Teleseismic P-wave tomography and mantle dynamics beneath Eastern Tibet, *Geochem. Geophys. Geosyst.*, **17**, 1861–1884.
- Li, C., van der Hilst, R. D., Engdahl, E. R. & Burdick, S., 2008. A new global model for P wave speed variations in Earth's mantle, *Geochem. Geophys. Geosyst.*, **9**(5), n/a, doi:10.1029/2007GC001806.
- Li, Z., Zuo, Y., Qiu, N. & Gao, J., 2017. Meso–Cenozoic lithospheric thermal structure in the Bohai Bay Basin, eastern North China Craton, *Geosci. Front.*, **8**, 977–987.
- Litasov, K. D., Ohtani, E., Sano, A., Suzuki, A. & Funakoshi, K., 2005. Wet subduction versus cold subduction, *Geophys. Res. Lett.*, **32**, 13312, doi:10.1029/2007GC001806.
- Liu, K. H., Gao, S. S., Silver, P. G. & Zhang, Y., 2003. Mantle layering across central South America, *J. geophys. Res.—Solid Earth*, **108**(B11), doi:10.1029/2007GC001806.
- Liu, Q., Zhang, L., Zhang, C. & He, L., 2016. Lithospheric thermal structure of the North China Craton and its geodynamic implications, *J. Geodyn.*, **102**, 139–150.
- Liu, X., Zhao, D., Li, S. & Wei, W., 2017. Age of the subducting Pacific slab beneath East Asia and its geodynamic implications, *Earth planet. Sci. Lett.*, **464**, 166–174.
- Lu, C., Grand, S. P., Lai, H. & Garnero, E. J., 2019. TX2019slab: a new P and S tomography model incorporating subducting slabs, *J. geophys. Res.—Solid Earth*, **124**, 11549–11567.
- Mao, Z., Lin, J. F., Jacobsen, S. D., Duffy, T. S., Chang, Y. Y., Smyth, J. R., Frost, D. J., Hauri, E. H. & Prakapenka, V. B., 2012. Sound velocities of hydrous ringwoodite to 16 GPa and 673 K, *Earth planet. Sci. Lett.*, **331–332**, 112–119, doi:10.1016/j.epsl.2012.03.001.
- Niu, Y. L., 2005. Generation and evolution of basaltic magmas: some basic concepts and a new view on the origin of Mesozoic–Cenozoic basaltic volcanism in eastern China, *Geol. J. China Universities*, **11**, 9–46.
- Obayashi, M., Yoshimitsu, J., Nolet, G., Fukao, Y., Shiobara, H., Sugioka, H., Miyamachi, H. & Gao, Y., 2013. Finite frequency whole mantle P wave tomography: improvement of subducted slab images, *Geophys. Res. Lett.*, **40**, 5652–5657.
- Pearson, D. G., *et al.* 2014. Hydrous mantle transition zone indicated by ringwoodite included within diamond, *Nature*, **507**, 221–224.
- Qiu, N., Zuo, Y., Chang, J. & Li, W., 2014. Geothermal evidence of Mesozoic–Cenozoic lithosphere thinning in the Jiyang sub-basin, Bohai Bay Basin, eastern North China Craton, *Gond. Res.*, **26**, 1079–1092.
- Revenaugh, J. & Sipkin, S. A., 1994. Seismic evidence for silicate melt atop the 410-km mantle discontinuity, *Nature*, **369**, 474–476.
- Ringwood, A. E., 1975. *Composition and Petrology of the Earth's Mantle*, MacGraw-Hill, p.618.
- Shen, X., Zhou, H. & Kawakatsu, H., 2008. Mapping the upper mantle discontinuities beneath China with teleseismic receiver functions, *Earth Planet Space*, **60**(7), 713–719.
- Si, S., Zheng, Y., Liu, B. & Tian, X., 2016. Structure of the mantle transition zone beneath the North China Craton, *J. Asian Earth Sci.*, **116**, 69–80.
- Sun, M., Gao, S. S., Liu, K. H. & Fu, X., 2020. Upper mantle and mantle transition zone thermal and water content anomalies beneath NE Asia: constraints from receiver function imaging of the 410 and 660 km discontinuities, *Earth planet. Sci. Lett.*, **532**, 116040, doi:10.1016/j.epsl.2019.116040.
- Tauzin, B., Debayle, E. & Wittlinger, G., 2010. Seismic evidence for a global low-velocity layer within the Earth's upper mantle, *Nat. Geosci.*, **3**(10), 718–721.
- Thio, V., Cobden, L. & Trampert, J., 2016. Seismic signature of a hydrous mantle transition zone, *Phys. Earth Planet. Inter.*, **250**, 46–63.
- Thompson, A. B., 1992. Water in the Earth's upper mantle, *Nature*, **358**(6384), 295–302.
- Tsuchiya, T., 2003. First-principles prediction of the P–V–T equation of state of gold and the 660-km discontinuity in Earth's mantle, *J. geophys. Res.—Solid Earth*, **108**, 2462, doi:10.1029/2003JB002446.
- Wang, X., Chen, Q. F., Niu, F., Wei, S., Ning, J., Li, J. & Liu, L., . . . &, 2020. Distinct slab interfaces imaged within the mantle transition zone, *Nature Geosci.*, **13**(12), 822–827.
- Wang, X. & Niu, F., 2011. Imaging the mantle transition zone beneath eastern and central China with CEArray receiver functions, *Earthq. Sci.*, **24**(1), 65–75.
- Wei, S. S. & Shearer, P. M. (2017). A sporadic low-velocity layer atop the 410 km discontinuity beneath the Pacific Ocean, *J. geophys. Res.—Solid Earth*, **122**, 5144–5159.
- Wood, B. J., Pawley, A. & Frost, D. R., 1996. Water and carbon in the Earth's mantle, *Phil. Trans. R. Soc. A.*, **354**, 1495–1511.
- Wu, F. Y., Yang, J. H., Xu, Y. G., Wilde, S. A. & Walker, R. J., 2019. Destruction of the North China craton in the Mesozoic, *Annu. Rev. Earth Planet. Sci.*, **47**, 173–195.
- Xu, W., Zheng, T. & Zhao, L., 2011. Mantle dynamics of the reactivating North China Craton: constraints from the topographies of the 410-km and 660-km discontinuities, *Sci. China Earth Sci.*, **54**(6), 881–887.
- Yan, D., Tian, Y., Zhao, D., Liu, C., Zhu, H. & Li, H., 2019. Upper mantle temperature structure of the North China Craton, *Phys. Earth planet. Int.*, **293**, 106269, doi:10.1016/j.pepi.2019.106269.
- Yang, J. & Faccenda, M., 2020. Intraplate volcanism originating from upwelling hydrous mantle transition zone, *Nature*, **579**, 88–91.
- Yang, J. H., Wu, F. Y., Wilde, S. A., Belousova, E. & Griffin, W. L., 2008. Mesozoic decratonization of the North China block, *Geology*, **36**, 467–470.
- Zhang, Y. Y., Chen, L., Wang, X. & Ai, Y. S., 2019. Lithospheric structure beneath the central and western North China Craton and adjacent regions from S-receiver function imaging, *Geophys. J. Int.*, **219**, 619–632.
- Zheng, X. F., Yao, Z. X., Liang, J. H. & Zheng, J., 2010. The role played and opportunities provided by IGP DMC of China National Seismic Network in Wenchuan earthquake disaster relief and researches, *Bull. seism. Soc. Am.*, **100**, 2866–2872.
- Zhu, F., Li, J., Liu, J., Dong, J. & Liu, Z., 2019. Metallic iron limits silicate hydration in Earth's transition zone, *Proc. Natl. Acad. Sci.*, **116**, 22526–22530.

SUPPORTING INFORMATION

Supplementary data are available at *GJI* online.

Please note: Oxford University Press is not responsible for the content or functionality of any supporting materials supplied by the authors. Any queries (other than missing material) should be directed to the corresponding author for the paper.